ACS APPLIED MATERIALS & INTERFACES

Research Article

www.acsami.org

# Self-Assembled Pillar-like Structures in Nanodiamond Layers by Pulsed Spray Technique

Grazia Cicala,*[,†] Alessandro Massaro,[†] Luciano Velardi,[†] Giorgio S. Senesi,[†] and Antonio Valentini[‡]

[†]CNR-IMIP, Via Amendola 122/D, 70126 Bari, Italy

[‡]Department of Physics, University of Bari, Via Orabona 4, 70126 Bari, Italy

Supporting Information

**ABSTRACT:** Pillar-like structures of nanodiamonds on a silicon substrate are self-assembled for the first time by a pulsed spray technique. This technique allows us to deposit nanodiamond layers by using high quality nanocrystals of 250 nm dispersed in 1,2-dichloroethane (DCE) solvent. The analysis of 2D/3D confocal and atomic force microscopy images evidences the presence of self-assembled pillar-like structures distributed in an irregular way. The proposed method is simple, easy and cheap, and does not require complex growth processes or structured materials, ideal for upscaling toward industrial biochip implementation and photonic applications. The suggested formation mechanisms of self-assembly are based on the so-called coffee stain effect, i.e., on the time evolution of DCE evaporation.

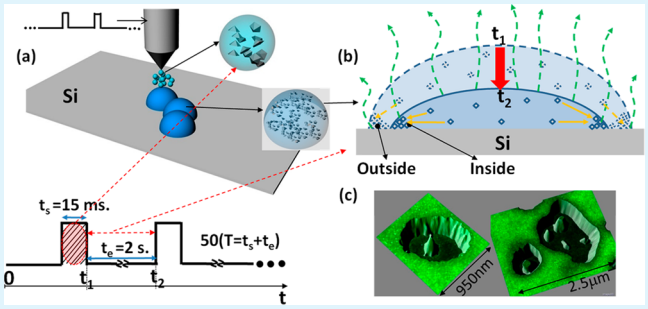


**KEYWORDS:** *diamond, nanoparticles, self-assembly, spray technique, pillar-like structures*

## INTRODUCTION

The fabrication of nanostructures, structured and aligned nanoparticles and nanodevices represents an important and hot topic in the nanotechnology field. Usually, the top-down and bottom-up approaches are followed to form and engineer the nanosystems mentioned above. The top-down technology is widely employed in the micro- and nanoelectronic industry, and uses e-beam lithography and reactive ion etching methods to go down to small sizes. Diamond nanowires[1] and nanopillars[2] for photonic devices are recent examples of a top-down nanofabrication starting from single-crystalline diamond. Contrarily, the bottom-up approach, very commonly used in the growth of aligned carbon nanotubes (CNTs)[3] and in natural biological systems, consists in the self-assembly of larger and complex systems starting from single units (atom, molecule, particle) by using various (grafting and spraying) methods. The formation of self-assembled structures depends critically on the physical and chemical environmental conditions employed. Recently, the self-assembly of octapod-shaped colloidal nanocrystals has been reported[4] and has been explained to be due to the solvent evaporation from poly(methyl methacrylate).

Typical examples of self-assembled structures are the architectures of ZnO nanowires on organized CNT able to generate photocurrent under UV irradiation,[5] and single spherical gold nanoparticles used as electromagnetic radiators.[6]

Diamond powders/nanoparticles of various sizes ranging from a few nanometers to tens of micrometers have been and are still used to treat the nondiamond substrates in order to enhance the nucleation process before the growth of thin diamond films by chemical vapor deposition (CVD) techniques such as microwave CVD[7] or hot filament CVD.[8] More recently, nondiamond substrates such as Si, AlN and sapphire, have been highly seeded using monodispersed nanodiamond (ND) particles. Specifically, the modification of nanodiamond surface makes them negatively or positively charged if annealed in oxygen or hydrogen, respectively, and allows to strongly affect the ND-substrate electrostatic interaction from repulsive to attractive.[9] In particular, a native silicon oxide layer (with negative $\zeta$-potential values) is omnipresent on the silicon wafer, thus the Si substrate presents a negative surface charge.[9]

Moreover, in the last years, ND particles have become widely available at low costs for a variety of synthesis techniques. They are ideal candidates for a wide range of applications as fillers for nanocomposites to improve the mechanical properties, in tribology, in mechanics because the ND particles are used as polishing material for the surface finish of watch sapphires, hard disks, etc., and in the biomedical field.[10]

The large surface area of NDs is suitable for adsorbing biomolecules. Many different functional groups can be attached to a ND surface, allowing quite sophisticated surface functionalizations[11] without compromising the properties of the diamond core. The presence of surface groups open many chances for the surface modification of ND. For example, further functionalization of amino groups permits us to graft DNA pieces on the coated ND particles.[10]

**Received:** September 2, 2014
**Accepted:** November 17, 2014
**Published:** November 17, 2014

  

The principal requirements for applying NDs in biomedical fields[12] are the stable dispersion in a selected liquid, the lower toxicity with respect to other carbon nanoparticles, the ability to attach drug[13] and biomolecules, and the high biocompatibility and ability to penetrate target tissues and cells.

ND particles are also proposed as a label for bioactive compounds if they include stable nitrogen/silicon-vacancies (N-V)/(Si-V) color centers.[14−18] These cause nonbleaching and nonblinking fluorescence in the red, which is a very important requirement for biolabeling purposes.

The large surface-to-volume ratio endows ND particles with higher surface reactivity than other forms of carbon, so that they have many other potential applications as a novel catalyst in the synthesis of styrene in mild conditions,[19] as electrode modified with a layer of detonation ND in electrochemical processes despite the insulating nature of nanoparticles.[20] Nanodiamond−$TiO_2$ composites can effectively degrade organic water pollutants by heterogeneous photocatalysis under ambient conditions. This process will reduce human impacts on freshwater systems.[21]

Moreover, researchers have studied other ND properties such as vacuum emission behavior,[22] the surface potential of diamond and gold NPs locally switched between negative and positive (via work functions of surrounding materials Si, Au and Pt).[23]

Diamond particles ranging from micro- to nanoscale can also be deposited on substrates using different techniques. Emi and Iizuka[24] produced diamond particles among nickel/copper particles using $CH_4/H_2$ radiofrequency plasmas. Grudinkin et al.[25] fabricated isolated spherical diamond particles "on synthetic opal" including Si-V color centers by means of CVD. Wang et al.[26] produced ND layers starting from aqueous solution of NDs by immersing glass substrates step by step.

Homogeneous coatings of different particle types can be directly deposited by means of a cold spray (CS) technique at high velocity using a carrier gas. The morphology of the layers deposited by CS depends on key parameters such as inlet pressure, temperature,[27] powder size,[28] particle impacting velocity[29] and substrate angle orientation.[30]

Recently, a spray technique simpler than CS has been utilized to obtain layers of multiwall CNTs previously dispersed in a solvent.[31,32]

In the present work, the pulsed spray technique was employed for ND layer fabrication. The evaporation of 1,2-dichlorethane (DCE) solvent from the ND dispersion sprayed on silicon substrate is a crucial point for the characteristics of the final layer. In the present experiments, in order to favor its evaporation the substrate temperature was set at 120 °C, a value greater than the boiling temperature of DCE (84 °C).

Further, key parameters, such as the time duration of spray pulse ($t_s$) and of solvent evaporation ($t_e$) and the spray period ($T = t_s + t_e$), were fixed to guarantee the repeatability of fabrication process.

The peculiarity and advantage of the proposed pulsed spray technique are the formation of ND self-assembly in pillar-like structures, obtained by the evaporation effect of dispersion drop. A detailed investigation of these structured ND layers was performed by Raman and photoluminescence spectroscopy, and 2D/3D confocal and atomic force microscopies, after the shape determination of the as-received ND particle. The main aim of this paper is to understand how the ND self-assembly is obtained, and to suggest and discuss the formation mechanism of the pillar-like structures.

## RESULTS

**Topography of a Single ND Particle, Chemical-Structural Characterization of ND Layers and Suggested Layout of ND-based Biochip Implementation.** The topography was measured by three-dimensional (3D) atomic force microscopy (AFM) on an as-received single ND particle, whereas the chemical-structural composition and impurity components were determined by Raman and photoluminescence (PL) spectroscopy on sprayed ND layers.

The 3D AFM image in Figure 1 shows a defined geometrical shape of a single 250 nm ND grain. This geometry recalls the typical truncated octahedral shape of diamond[33] as shown in the inset.

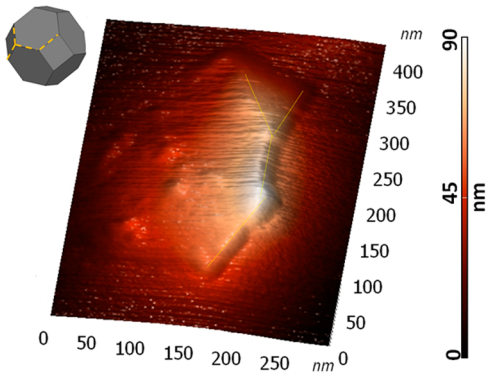


**Figure 1.** AFM 3D topography image of a single nanodiamond particle. The dashed lines correspond to crystal edges (the inset shows the 3D model truncated octahedral crystal).

The sharp diamond ($sp^3$ bonded carbon) peak at 1332 $cm^{-1}$ and the very weak graphite ($sp^2$ bonded carbon) band centered at 1574 $cm^{-1}$ of the Raman spectrum,[34] shown in Figure 2a, indicate the high quality of the sprayed ND layer.

The PL spectrum in Figure 2b shows the zero-phonon lines (ZPL) of N-$V^0$ and N-$V^-$ centers peaked at 575 and at 637 nm, respectively;[35] its inset is the zoomed peak of the N-$V^-$ color center. The dominant broad band, on which are overlapped the Si substrate and diamond peaks, is due to the phonon sideband of the N-V centers ZPL.

The N-$V^-$ line is usually the most studied color center because of its stable photoluminescence at room temperature. It is of great interest as a single-atom quantum probe for nanoscale processes. Recently, some authors[36] have studied theoretically the quantum behavior of a N-V probe in a complex biological environment. Moreover, the emission frequency is potentially useful for quantum computation[37] and biochip implementations.

Examples of simple biochip on glass and silicon substrates are depicted in the photos reported in Figure 3a,b, respectively, where sprayed ND spots are arranged by means of a mask in an array configuration suitable for bioapplications.[10]

To use the chip as a biosensor, it is necessary to modify the diamond surface with hydrogen, oxygen and $-NH_2$ groups,[11] and successively to functionalize[11,38] it with proteins, polymers, DNA and so on. Phenyl linker molecules can be attached electrochemically on NDs in order to detect the CK20 cancer (colorectal cancer[39]) marker for the DNA gene sensor platform.[38] The ND surface functionalization can be performed by means of 4-nitrophenyl diazonium tetrafluoroborate[11,38] after a pretreatment ND hydrogenation process.[11]

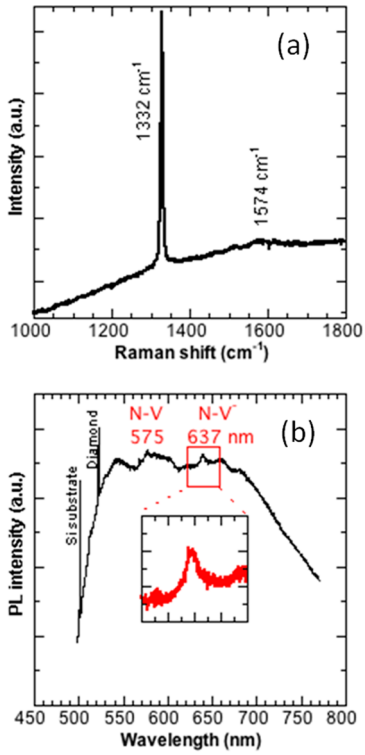


**Figure 2.** (a) Raman and (b) photoluminescence spectra of a sprayed ND layer.

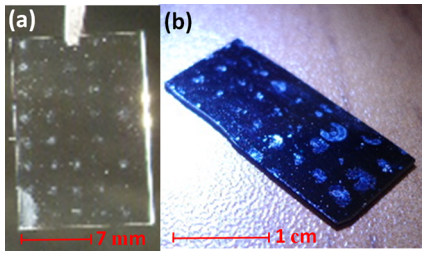


**Figure 3.** Photos of suggested layout of a biochip on (a) glass and (b) silicon substrates, based on arrays of sprayed ND spots obtained by a mask.

**ND Layer Analysis by AFM.** The morphology of the ND layers was characterized by means of the AFM technique. A picture of a sprayed ND layer is shown in Figure 4 and highlights the typical distribution of fine diamond particles on a silicon substrate (12 × 12 $mm^2$ size) where a quasi-homogeneous thick film in the central region, and a thin noncontinuous layer at the edges of the sample can be observed. Figure 4 also shows a series of AFM two-dimensional (2D) 10 × 10 $\mu m^2$ images acquired following the arrow direction. Figure 4 includes the AFM 2D topography images (a, b, c, d, e, f) on the left, and the corresponding 2D phase images (a′, b′, c′, d′, e′, f′) on the right. The sequence of both images describes the spatial evolution of the ND layers, moving from the external edge to the middle of the sample with steps of 1 mm. The morphological analysis has been carried out on the phase images because of their better contrast. The a′ and b′ images denote the presence of isolated particles or initial agglomerates of various sizes, whereas the c′, d′ and e′ images show a coalescence of agglomerates together with a more extended coverage on the silicon substrate. Finally, the f′ image, corresponding to the central region of the sample, shows a

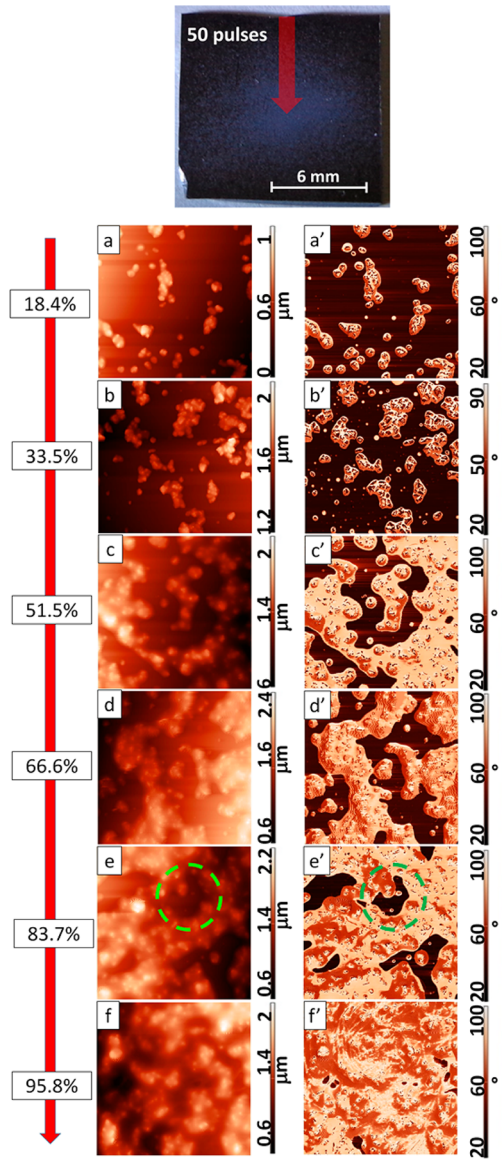


**Figure 4.** Picture of a sprayed ND layer on p-Si substrate. (a–f) AFM 2D topography images, and (a′–f′) corresponding 2D phase images on 10 × 10 $\mu m^2$ area of ND layer. The spatial evolution, with steps of 1 mm, is performed by following the red arrows. The surface coverage (in %) is reported on the red arrow at each position.

quasi-homogeneous ND layer. The surface coverage, evaluated using the ImageJ software by means of the Fiji tool as a function of position on the sample surface, varies from 18.4 to 95.8%.

Figure 5a,b shows 3D AFM topography images for two different areas of the ND layer in which one microcavity is present. Figure 5a is a zoomed region of Figure 4e′. The 5a′ and 5b′ profiles represent a linear scan along the red lines (crossing the microcavity) indicated in 3D topography images a and b. The a′ and b′ scan outcomes reveal two and one vertical pillar-like structures of ND inside each explored microcavities, respectively. Specifically, Figures 5a′ and 5b′ show a conical shape of these pillar-like structures that are (a′) higher and (b′) lower than the surrounding ND layer. A careful inspection of the pillars reveals that their diameters are of the order of the ND grain size (around 250 nm), whereas in Figure 5b′, the


dx.doi.org/10.1021/am505974d | ACS Appl. Mater. Interfaces 2014, 6, 21101–21109

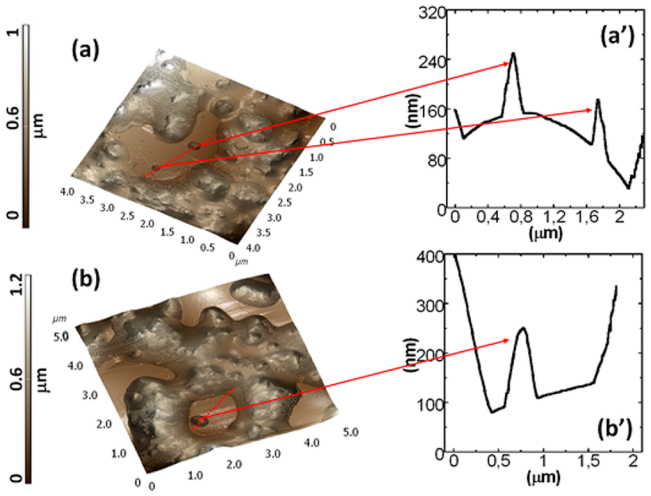


**Figure 5.** (a,b) AFM 3D topography images for two different areas of the ND layer; (a′,b′) profiles of the scan along the red lines, showing the presence of two and one pillars, respectively.

pillar at the bottom is about 500 nm wide, i.e., two particles wide.

**ND Layer Analysis by Confocal Microscopy.** Thanks to the photoluminescence properties of the ND, the morphological characterization of the sprayed ND layer was also carried out by confocal microscopy. This technique permits also to acquire 3D *z*-stack images that are obtained by defining an inferior and superior limit, corresponding to the focusing of the silicon/ND layer interface and the top of the ND film surface, respectively.

Obviously, a 3D *z*-stack image cannot be directly observed, but it is composed of many images recorded at different *z*-sections, which allow us to get spatial information along the film thickness. Each image of Figure 6a–f represents a slice of a 3D *z*-stack image along the ND layer thickness, starting from (a) the silicon/ND layer interface to (f) the top of the ND film surface. The analysis of these images allows to provide information on the topography of the ND film at different *z*-sections, i.e., to study the evolution of the morphology along the thickness. Initially, at low *z*-values, the image luminescence is low due to the presence of the underlying silicon substrate uncoated and coated with a very thin ND layer (dark region) and some emitting ND clusters/agglomerates (Figure 6a), then the ND agglomerates start to grow generating a noncontinuous layer with increasing *z*-value (Figures 6b,c). For the highest *z*-value (Figure 6f), the ND layer is continuous, but the thickness is highly irregular showing mounts and valleys. The pointed out cavities, i.e., valleys (Figure 6f), correspond to the positions of the ND clusters formed initially (Figure 6a).

A typical confocal 2D image of the ND layer surface covering an area of 246 × 246 $\mu m^2$ is shown in Figure 7a. Similarly to

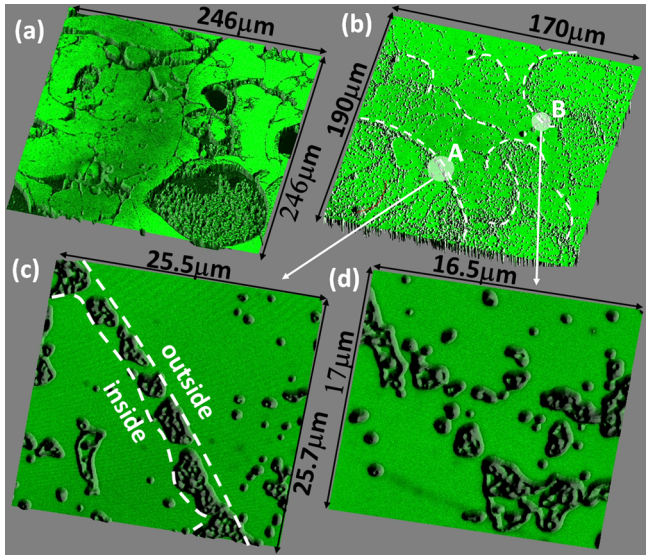


**Figure 7.** (a–d) Typical confocal 2D images of the ND layer surface at different magnifications.

Figure 6f, the ND layer is continuous but irregular. In particular, many circles of different size are observed. The image in Figure 7b evidences better the boundaries of these circles, which are due to the drying process, i.e., the evaporation of the dispersion drops sprayed during the deposition process. Figure 7c,d illustrates the circular boundaries zoomed regions, A and B of Figure 7b and show the presence of microcavities along the drop edges or contact line.

The 2D confocal image reported in Figure 8a shows an area of 27 × 27 $\mu m^2$ of a quasi-homogeneous ND layer with many isolated pillar-like ND structures. The processed 3D images in Figure 8b–g are zoomed regions of Figure 8a, which well depict the self-assembly of single or many pillar-like structures

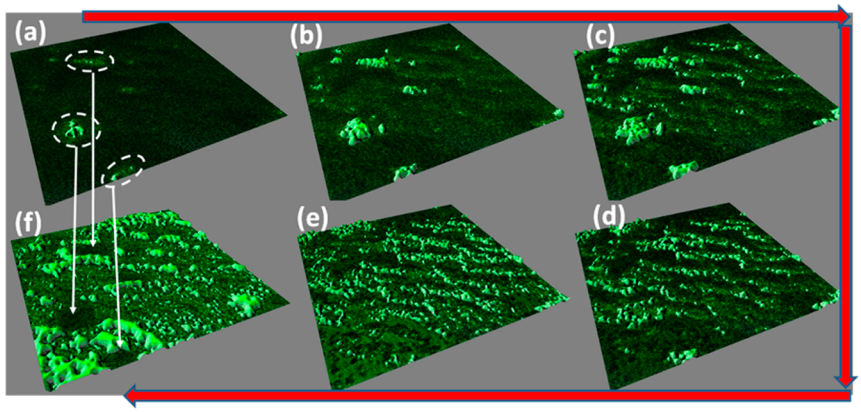


**Figure 6.** (a–f) Confocal microscopy raster scans (52 × 52 $\mu m^2$) of ND layer. The red arrows indicate the *z*-position from (a) the substrate/ND layer interface to (f) the ND layer surface.

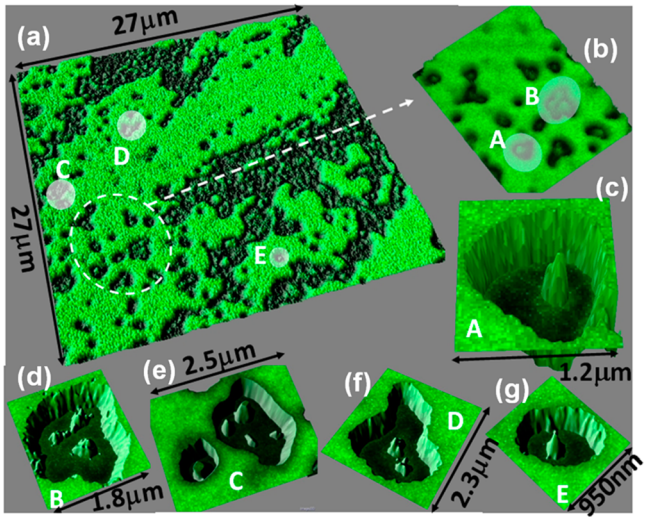


**Figure 8.** (a) Confocal 2D image of a quasi-homogeneous ND layer with many isolated pillar-like ND structures. (b–g) Processed 3D images of zoomed areas of image a.

inside the microcavities. These measurements confirm the previous AFM results in Figure 5. A careful observation of the processed 3D images reveals that the height values of the pillars are lower, the same or higher than that of the surrounding ND layer.

The confocal image reported in Figure 9 is of crucial importance because at the same time is giving information on

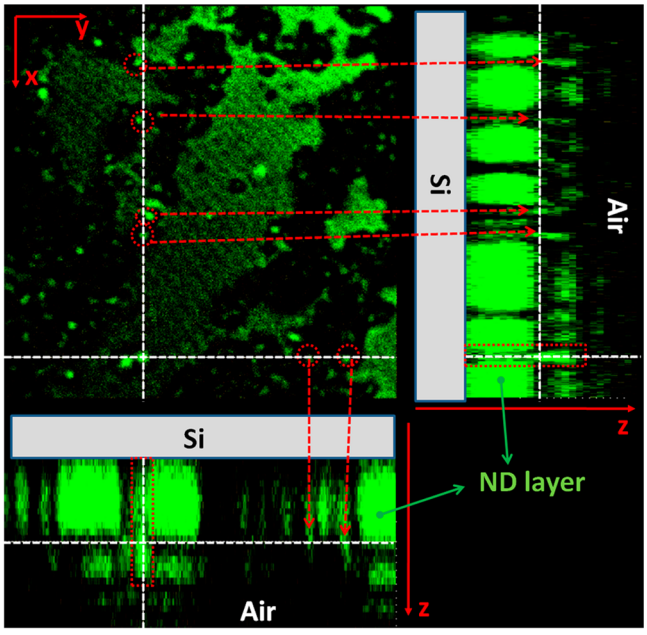


**Figure 9.** 3D *z*-stack confocal image proving the presence of ND pillar-like structures. The image in the *x*-*y* plane covers an area of 16 × 16 $\mu m^2$, the height of *z*-*x* and *z*-*y* planes is 15 $\mu$m.

morphology in plane (*x*-*y*) but also in sections (*z*-*x* and *z*-*y*). The upper-left image (16 × 16 $\mu m^2$ area) of Figure 9 shows the *x*-*y* plane of the 3D *z*-stack image, one of the frames acquired during the *z*-scan. The upper-right and the bottom-left images of Figure 9 represent the *z*-*x* and *z*-*y* planes corresponding to the white vertical and horizontal dashed lines of the *x*-*y* plane, respectively. These planes are obtained from the union of the *z*-sections acquired during the scan ($\Delta z$ = 15 $\mu$m), and well highlight the presence of silicon substrate, bulk ND layer and pillar-like structures within microcavities of various sizes. In particular, the *z*-*y* plane image well reveals the presence of isolated pillar-like structures on silicon substrate, in regions without ND layer (where the droplet evaporation occurs, as explained in the next section).

## DISCUSSION

**Formation Mechanisms of Self-Assembly Pillar-like Structures in Sprayed ND Layers.** The fundamental principles of the ND layer deposition by spray technique are based on the use of ND particle dispersion in DCE solvent that is blown or driven onto the substrate through the pulsed ultrasonic atomizer in the form of tiny drops (performed within the spray pulse of $t_s$ = 15 ms), and the solvent evaporation at a defined temperature during the $t_e$ = 2s between two pulses, as reported in the sketches of Figure 10a,b. When the solvent in a drop of this dispersion evaporates from the silicon substrate surface, most of the particles are deposited in a ring-like way, as shown in the optical microscopy image and AFM inset of Figure 10d. This phenomenon is commonly observed during the evaporation of a coffee drop and it is known as the coffee stain effect.[40]

If the substrate surface is hydrophilic[41] with respect to the solvent or the dispersion, during the entire drying process the drop edges are pinned to the substrate and an outward flow (which is a function of the ND density)[42] develops in the liquid. This outward capillary flow drags the ND particles toward the contact line, leading to the development of a solute ring on the substrate (see Figure 7b). As the evaporation proceeds, the particles replenish the edges forming a ring-like deposit on the substrate. On the contrary, if the substrate surface is hydrophobic[43] with respect to the solvent or the dispersion, the solute ring does not form because the solvent flows toward the center of the droplet. Consequently, a uniform deposition of particles is obtained.

To establish the hydrophilic or hydrophobic behavior, wettability measurements of DCE dispersion on silicon substrate and on previously deposited ND layer were carried out. The contact angles $\theta$ resulted 29° (Figure 10c) and 18° in the first and second case, respectively, denoting a hydrophilic character. Details of the contact angle measurements are available in the Supporting Information. The reduction of the drop height (Figure 10b) during the evaporation is easily observed and causes a variable contact angle achieving zero value when the evaporation ends. The entire evaporative process was filmed and allowed us to follow the evolution of the drop geometry, the deposit formation and the dynamics of the particles migration. The side-views images (e.g., Figure 10c) are used to calculate the contact angle, volume, radius, and height of the drop at each instant by the use of a homemade code.

These results explain why, in the present experiments, the coffee stain effect is dominant. For the DCE solvent evaporation, a very thin solvent residue is observed, whereas for the ND dispersion evaporation a thicker layer of particles is formed. By zooming-in on the ring stain, a nonhomogeneous particle arrangement is observed in the optical image of Figure 10d. Going from the external to the internal ring stain, there is a remarkable transition from an ordered (more dense and compact) to a disordered (random and sparse) arrangement. This phenomenon has been described by Marin et al.[44] as rush-

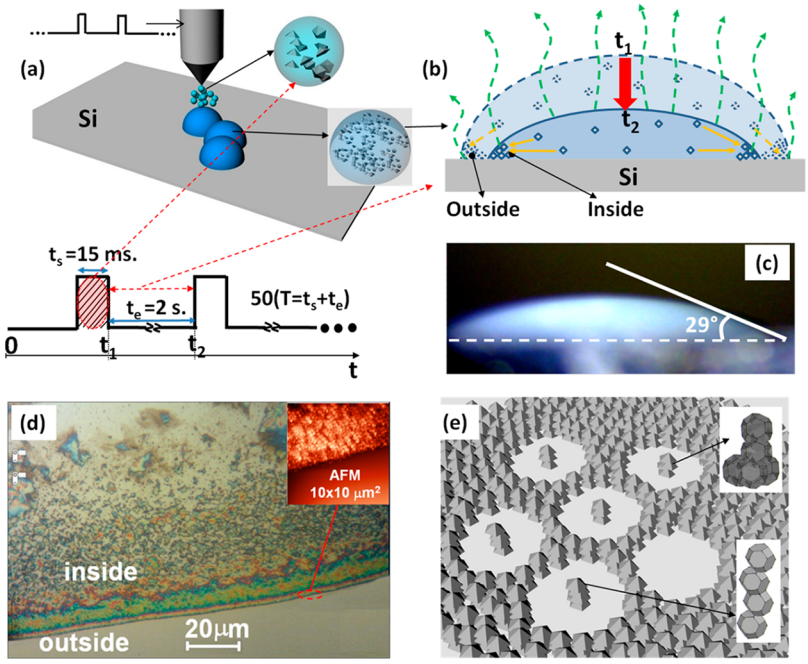


**Figure 10.** (a) Sketch of pulsed spray technique. (b) ND dispersion droplet evaporation. (c) Side view image of a ND dispersion drop. (d) Optical microscopy image (500×) of a ring stain region, the inset is an AFM image of the external boundary. (e) 3D model for the formation of pillar-like structures.

hour because the particle velocity was shown to increase drastically in the last moment of the droplet's life. Indeed, the particles that arrive early at low deposition speed form an ordered structure (inset of Figure 10d), whereas particles that arrive during the rush-hour have a high speed and form a disordered phase.

On the basis of the results shown in Figure 6e,f, it is evident that, although the ND layer is continuous, its thickness is highly nonuniform exhibiting mounts and valleys. This result is mainly due to the chaotic nature of the deposition process that consists in droplets sprayed on the silicon surface, and successive solvent evaporation for 50 periods (Figure 10a).

Images a and b in Figure 7, relative to areas of a ND thick layer, also evidence the presence of overlapped ring-like perimeters of various dimensions, which are representative of the periphery of drying drops and have different sizes where the coffee stain mechanism is operative. The big ones can be formed by coalescence of droplets distributed with high density. By zooming in the ring perimeter (images c and d in Figure 7), a structured stain, which is more aligned outside with respect to the inside region, is clearly observed. Similarly to the phenomenon shown in Figure 10d, the rush-hour behavior[44] is also found at the top of the ND layer surface.

A detailed analysis of the vertical structures is illustrated in Figures 8 and 9, denoting the presence of self-assembled pillar-like structures obtained with the last programmed pulse and the complete evaporation of the DCE solvent. These structures are formed by ND losses that occur due to the capillary flow toward the drop edge during the solvent evaporation and successive pulses. The additional droplets, containing ND particles, could land in the middle of the microcavities (generated by the coffee stain effect), and the deposition of further NDs lengthens the pillars. Additionally, both Figures 8 and 9 show that the self-assembly of pillar-like structure is formed either on an already deposited ND layer or at the substrate/ND layer interface. This last was also well observed in the 3D AFM topography images in Figure 5a,b. On the basis of the obtained results and formulated hypotheses, a schematic representation of the self-assembly mechanisms of the pillar-like structures in ND layers is illustrated in the sketch of Figure 10e.

## CONCLUSIONS

A pulsed spray technique able to deposit ND layers is presented and discussed. 2D/3D AFM and confocal images permit us to observe ND self-assembled pillar-like structures by a deep investigation of the layer surface. The formation of these structures has been explained on the basis of the complex solvent evaporation processes occurring at the temperature of 120 °C. Both images of confocal and atomic force microscopies have shown the presence of single or multiple pillars in microcavities of different sizes and shapes. The peculiarity of these structures could be employed in photonic, biosensing and bioimaging applications, also thanks to the N-V color centers observed in the produced ND layer as revealed by the photoluminescence spectrum. Future investigations will be focused on the control of the self-assembly processes.

## MATERIALS AND METHODS

**Pulsed Spray Technique.** ND layers were produced by means of the pulsed spray technique, which is a relatively simple approach to deposit particles onto a substrate by evaporation of a dispersion droplet. The advantages of this technique are its inherent flexibility and the possibility of depositing very small amounts of material. A quantity of 30 mg of natural ND particles (grain size 250 nm, ElementSix) was dispersed in 30 mL of the apolar solvent 1,2-dichloroethane by sonication for 30 min by a Bandelin Sonoplus HD2070 system. Immediately after, the dispersion was sprayed onto a piece of 12 × 12 $mm^2$ p-doped Si substrate (previously cleaned for 5 min in isopropyl alcohol by ultrasound bath). The setup used for the sprayed dispersion consisted of an ultrasonic atomizer, a heater and a PC interfaced to the system. The atomizer was fixed at a constant distance of 18 mm from the substrates set on a holder heated at 120 °C during the deposition, to evaporate easily the DCE solvent. The dispersion of fine diamond

particles was propelled through the nozzle as liquid jet. An acoustic pulse ejected dispersion droplets from a dispenser. The pulse was generated piezoelectrically (microsolenoid valve) and controlled via software. The time duration of the spray pulse was set at $t_s$ = 15 ms and the time between two pulses, the solvent evaporation time ($t_e$), was 2 s. The spray period was $T = t_s + t_e$. The investigated samples were obtained with 50 spray periods, see Figure 4. The deposited ND layers exhibited a good adhesion because van der Waals interactions closely packed the fine particles, as reported in the Supporting Information.

The suggested layout of preliminary biochip prototypes illustrated in Figure 3a,b was obtained by means of a single spray period using a mask placed directly on the glass/silicon substrates heated at 120 °C.

**3D Confocal Microscopy Technique.** Confocal fluorescence scanning was carried out using a Leica TSC SP5 system, which includes a fluorescence microscope with inverted stand, the confocal part, the scan head, the laser optics and the computer. The confocal microscope offered the possibility to select up to eight laser lines: 405 nm (blue diode), 476, 488, 496, 514 nm (argon-ion), 543, 594, 633 nm (helium neon1, helium neon2, helium neon3, respectively). A 488 nm line of an Ar-ion laser was employed to illuminate the ND layer through a 63x 0.95 numerical aperture (NA) oil immersion objective. A proper oil drop with a refractive index of $n$ = 1.518 was used to reduce the spherical aberration. The sample was set on a computer controller stage equipped with a *x-y-z* closed loop positioner. The laser power was set at 20% and the smart gain was tuned in order to overcome the problem of saturation effect of the image intensity.

The LAS AF software of the Leica TSC SP5 system permitted us to acquire single images that are a snapshot of data in a single *x-y* plane. 3D *z*-stack modality added the third dimension setting the *z*-values for the beginning and the end of sampling. Thus, a 3D image projection was obtained by assembling the series of images at various focal planes. The 2D and 3D images were acquired observing the fluorescent ND layer in the wavelength range from 550 to 660 nm, through the filter RT30/70. The final images were postprocessed by the 3D tool of Image-J software.

**AFM Technique.** An NTEGRA Aura scanning probe microscope (NT-MDT, Zelenograd, Moscow, Russia) was employed, placed on an antivibrating table to reduce interferences from building vibrations. All AFM surface images were obtained in ambient conditions and were acquired in noncontact mode either as topographies, which showed the height of contours to evaluate the surface topography, or as phase images that highlight the fine features to provide more information on sample heterogeneity and to obtain material-properties information. Topographical AFM images typically are color coded by showing elevated areas in bright (here bright yellow) and lower areas in dark (here dark brown). No smoothing has been applied to the images, and consequently to the profiles. AFM maps were acquired using commercial, high accuracy noncontact polysilicon probe tips with high reflectivity golden coating at a resonance frequency of 235 kHz.

To increase the representativeness of the whole sample, five areas of the surface were scanned for each sample using different spatial resolutions. A typical scan size area, 10 × 10 $\mu m^2$, was examined in further details. Images were then processed and elaborated also as profiles and 3D topography through the Nova software. Further, the shape of a single natural 250 nm ND particle was determined by attaching the powder on a biadhesive tape as the substrate.

**Raman Spectroscopy.** The Raman and photoluminescence (PL) spectra were measured at room temperature by means of a Raman confocal micro spectrometry apparatus (Labram from Jobin−Yvon Horiba) in the backscattering configuration. The spectra were determined by photoexciting the ND layer with a 488 nm line of an Ar-ion laser. Raman signals were obtained by focusing the laser on the ND layer with a 100× objective, probing a spot size beam of 1 $\mu$m. The Raman signal was sent into a spectrometer equipped with a 1800 grooves/mm grating. The laser output power was set at 4.5 mW, and the collection time was 1 s. The PL signal was detected by means of a 10× objective focusing the laser beam in 10 $\mu$m spot size and using a spectrometer equipped with 600 grooves/mm grating. The laser output power was set at 12 mW, and the collection time was 1 s. The PL signals were then averaged over ten spectra. Both Raman and PL signals were detected by means of a cooled CCD.

**Contact Angle Measurements.** The contact angle $\theta$ was measured by a CCD camera. A fast-camcorder connected to the computer permitted to record images and videos during the drop casting on the substrate. All video frames were analyzed using a homemade software based on the droplet contour reconstruction by B-spline method and the contact angle was measured by the following equation:

$$\theta = 2\arctan(h/r) \quad (1)$$

where $h$ is the height of the drop and $r$ is the radius of the drop base.

## ■ ASSOCIATED CONTENT

### Ⓢ Supporting Information

Typical dispersions of 250 nm nanodiamond (ND) particles in the 1,2-dichlorethane (DCE) solvent; contact angle measurements at different evaporation times for a droplet of dispersion on Si substrate and on ND layer; dependence of the van der Waals force on the particle size and interaction distance. This material is available free of charge via the Internet at http://pubs.acs.org.

## ■ AUTHOR INFORMATION

### Corresponding Author

*Dr. Grazia Cicala. E-mail: grazia.cicala@imip.cnr.it.

### Author Contributions

The paper was written through contributions of all authors. All authors have given approval to the final version of the paper.

### Notes

The authors declare no competing financial interest.

## ■ ACKNOWLEDGMENTS

This study was carried out within the framework of the Project PON03PE_00067_6 “APULIA SPACE”, (Italy). The authors are grateful to Prof. G. Carbone of Politecnico di Bari, Italy for the use of the AFM instrument, Dr. G. Perna and Prof. V. Capozzi of University of Foggia, Dipartimento di Scienze Biomediche for Raman spectroscopy measurements and Mr D. Marzulli of CNR-IBBE UOS for confocal microscope measurements.

## ■ ABBREVIATIONS

AFM = atomic force microscopy
CNTs = carbon nanotubes
CS = cold spray
CVD = chemical vapor deposition
DCE = 1,2-dichlorethane
N-V = nitrogen vacancy
ND = nanodiamond
PL = photoluminescence
Si-V = silicon vacancy
ZPL = zero-phonon line

## ■ REFERENCES

(1) Babinec, T. M.; Hausmann, B. J. M.; Khan, M.; Zhang, Y.; Maze, J. R.; Hemmer, P. R.; Loncar, M. A Diamond Nanowire Single-Photon Source. *Nat. Nanotechnol.* **2010**, *5*, 195−199.

(2) Neu, E.; Appel, P.; Ganzhorn, M.; Sanchez, J. M.; Lesik, M.; Mille, V.; Jacques, V.; Tallaire, A.; Achard, J.; Maletinsky, P. Photonic Nano-structures on (111)-Oriented Diamond. *Appl. Phys. Lett.* **2014**, *104*, 153108-1−153108-4.

(3) Askari, D.; Ghasemi-Nejhad, M. N. Effects of Vertically Aligned Carbon Nanotubes on Shear Performance of Laminated Nano-

composite Bonded Joints. *Sci. Technol. Adv. Mater.* **2012**, *13*, 045002-1−045002-10.
(4) Arciniegas, M. P.; Kim, M. R.; De Graaf, J.; Brescia, R.; Marras, S.; Miszta, K.; Dijkstra, M.; Van Roy, R.; Manna, L. Self-Assembly of Octapod-Shaped Colloidal Nanocrystals into a Hexagonal Ballerina Network Embedded in a Thin Polymer Film. *Nano Lett.* **2014**, *14*, 1056−1063.
(5) Ok, J. G.; Tawfick, S. H.; Juggernauth, K. A.; Sun, K.; Zhang, Y.; Hart, A. J. Electrically Addressable Hybrid Architectures of Zinc Oxide Nanowires Grown on Aligned Carbon Nanotubes. *Adv. Funct. Mater.* **2010**, *20*, 2470−2480.
(6) Massaro, A. Light Coupling and Directional Emission of Spherical Gold Nanoparticles as Nanosensors. *Opt. Quant. Electron.* **2012**, *44*, 227−233.
(7) Cicala, G.; Magaletti, V.; Senesi, G. S.; Tamborra, M. Smoothness Improvement of Micrometer- and Submicrometer-Thick Nanocrystalline Diamond Films Produced by MWPECVD. *J. Nanopart. Res.* **2013**, *15*, 1549-1−1549-14.
(8) Buijnsters, J. G.; Vàzquez, L. Growth Dynamics of Nanocrystalline Diamond Thin Films Deposited by Hot Filament Chemical Vapor Deposition: Influence of Low Sticking and Renucleation Processes. *J. Phys. Chem. C* **2011**, *115*, 9681−9691.
(9) Shimoni, O.; Crvenka, J.; Karle, T. K.; Fox, K.; Gibson, B. C.; Tomljenovic-Hanic, S.; Greentree, A. D.; Prawer, S. Development of a Templated Approach to Fabricate Diamond Patterns on Various Substrates. *ACS Appl. Mater. Interfaces* **2014**, *6*, 8894−8902.
(10) Mochalin, V. N.; Shenderova, O.; Gogotsi, D. H. Y. The Properties and Applications of Nanodiamonds. *Nat. Nanotechnol.* **2012**, *7*, 11−23.
(11) Arnault, J. C.; Petit, T.; Girard, H.; Chavanne, A.; Gesset, C.; Sennour, M.; Chaigneau, M. Surface Chemical Modifications and Surface Reactivity of Nanodiamonds Hydrogenated by CVD Plasma. *Phys. Chem. Chem. Phys.* **2011**, *13*, 11481−11487.
(12) Shrand, A. M.; Hens, S. A. C.; Sherendova, O. A. Nanodiamonds Particles: Properties and Perspectives for Bioapplications. *Crit. Rev. Solid State Mater. Sci.* **2009**, *34*, 18−74.
(13) Ōsawa, E.; Ho, D. Nanodiamond and its Application to Drug Delivery. *J. Med. Allied Sci.* **2012**, *2*, 31−40.
(14) Gruber, A.; Dräbenstedt, A.; Tietz, C.; Fleury, L.; Wrachtrup, J.; von Borczyskowski, C. Scanning Confocal Optical Microscopy and Magnetic Resonance on Single Defect Centers. *Science* **1997**, *276*, 2012−2014.
(15) Fu, C.-C.; Lee, H.-Y.; Chen, K.; Lim, T.-S.; Wu, H.-Y.; Lin, P.-K.; We, P.-K.; Tsao, P.-H.; Chang, H.-C.; Fann, W. Characterization and Application of Single Fluorescent Nanodiamonds as Cellular Biomarkers. *Proc. Natl. Acad. Sci. U. S. A.* **2007**, *104*, 727−732.
(16) Vlasov, I. I.; Barnard, A. S.; Ralchenko, V. G.; Lebedev, O. I.; Kanzyuba, M. V.; Saveliev, A. V.; Konov, V. I.; Goovaerts, E. Nanodiamond Photoemitters Based on Strong Narrow-Band Luminescence from Silicon-Vacancy Defects. *Adv. Mater.* **2009**, *21*, 808−812.
(17) Singh, S.; Catledge, S. A. Silicon Vacancy Color Center Photoluminescence Enhancement in Nanodiamond Particles by Isolated Substitutional Nitrogen on {100} Surfaces. *J. Appl. Phys.* **2013**, *113*, 044701-1−044701-6.
(18) Bradac, C.; Gaebel, T.; Naidoo, N.; Sellars, M. J.; Twamley, J.; Brown, L. J.; Barnard, A. S.; Plakhotnik, T.; Zvyagin, A. V.; Rabeau, J. R. Observation and Control of Blinking Nitrogen Vacancy Centres in Discrete Nanodiamonds. *Nat. Nanotechnol.* **2010**, *5*, 245−249.
(19) Zhang, J.; Su, D. S.; Blume, R.; Schlögl, R.; Wang, R.; Yang, X.; Gajovic, A. Surface Chemistry and Catalytic Reactivity of a Nanodiamond in the Steam-Free Dehydrogenation of Ethylbenzene. *Angew. Chem., Int. Ed.* **2010**, *49*, 8640−8644.
(20) Varley, T. S.; Hirani, M.; Harrison, G.; Holt, K. B. Nanodiamond Surface Redox Chemistry: Influence of Physicochemical Properties on Catalytic Processes. *Faraday Discuss.* **2014**, DOI: 10.1039/c4fd00041b.
(21) Pastrana-Martínez, L. M.; Sergio Morales-Torres, S.; Carabineiro, S. A. C.; Buijnsters, J. G.; Faria, J. L.; Figueiredo, J. L.; Silva, A. M. T. Nanodiamond−$TiO_2$ Composites for Heterogeneous Photocatalysis. *ChemPlusChem* **2013**, *78*, 801−807.
(22) Hsu, S. H.; Kang, W. P.; Raina, S.; Huang, J. H. Nanodiamond Vacuum Field Emission Device with Gate Modulated Triode Characteristics. *Appl. Phys. Lett.* **2013**, *102*, 203105-1−203105-5.
(23) Stehlik, S.; Petit, T.; Girard, H. A.; Kromka, A.; Arnault, J.-C.; Rezek, B. Surface-Modified Diamond and Gold Nanoparticles Exchange Charge and Switch Polarity with Substrates. *J. Nanopart. Res.* **2014**, *16*, 2364−2374.
(24) Emi, J.; Iizuka, S. Diamond Particles Deposited among Nickel/Copper Particles in Energy Controlled $CH_4/H_2$ RF Discharge Plasmas. *J. Surf. Eng. Mater. Adv. Technol.* **2012**, *2*, 158−162.
(25) Grudinkin, S. A.; Feoktistov, N. A.; Bogdanov, K. V.; Baranov, M. A.; Baranov, A. V.; Fedorov, A. V.; Golubev, V. G. Chemical Vapor Deposition of Isolated Spherical Diamond Particles with Embedded Silicon−Vacancy Color Centers onto the Surface of Synthetic Opal. *Semiconductors* **2014**, *48*, 268−271.
(26) Wang, H.-D.; Yang, Q.; Hui Niu, C. Preparation of Films of Nanodiamonds by Step-by-Step Deposition Approach through Hydrogen Bonding. *Diamond Relat. Mater.* **2012**, *25*, 73−79.
(27) Wang, Q.; Birbilis, N.; Zhang, M. X. Process Optimisation of Cold Spray Al Coating on AZ91 Alloy. *Surface Eng.* **2014**, *30*, 323−328.
(28) Jeandin, M.; Rolland, G.; Descurninges, L. L.; Berger, M. H. Which Powders for Cold Spray? *Surface Eng.* **2014**, *30*, 291−298.
(29) Lupoi, R. Current Design and Performance of Cold Spray Nozzles: Experimental and Numerical Observations on Deposition Efficiency and Particle Velocity. *Surface Eng.* **2014**, *30*, 316−322.
(30) Li, W. Y.; Zhang, D. D.; Huang, C. J.; Yin, S.; Yu, M.; Wang, F. F.; Liao, H. L. Modelling of Impact Behaviour of Cold Spray Particles: Review. *Surface Eng.* **2014**, *30*, 299−308.
(31) Jeong, H. J.; Choi, H. K.; Kim, G. Y.; Song, Y. I.; Tong, Y.; Lim, S. C.; Lee, Y. H. Fabrication of Efficient Field Emitters with Thin Multiwalled Carbon Nanotubes using Spray Method. *Carbon* **2006**, *44*, 2689−2693.
(32) Melisi, D.; Nitti, M. A.; Valentini, M.; Valentini, A.; Ditaranto, N.; Cioffi, N.; Di Franco, C. Radiation Detectors Based on Multiwall Carbon Nanotubes Deposited by a Spray Technique. *Thin Solid Films* **2013**, *543*, 19−22.
(33) Silva, F.; Bonnin, X.; Achard, J.; Brinza, O.; Michau, A.; Gicquel, A. Geometric Modeling of Homoepitaxial CVD Diamond Growth: I. The {100}{111}{110}{113} System. *J. Cryst. Growth* **2008**, *310*, 187−203.
(34) Cicala, G.; Brescia, R.; Nitti, M. A.; Romeo, A.; Ambrico, M.; Schiavulli, L.; Terna, G.; Capozzi, V. Thermoluminescent Response of Thin (2 mm) Polycrystalline Diamond Film Grown by Pulsed and Continuous Microwave Plasmas. *Diamond Relat. Mater.* **2010**, *19*, 470−473.
(35) Bradac, C.; Gaebel, T.; Rabeau, G. R. In *Optical Engineering of Diamond*; Miltren, R. D., Rabeau, J. R., Eds.; Wiley-VCH Verlag & Co. KGaA: Berlin, 2013; Chapter 5.
(36) Hall, L. T.; Hill, C. D.; Cole, J. H.; Städler, B.; Caruso, F.; Mulvaney, P.; Wrachtrup, J.; Hollenberg, L. C. L. Monitoring Ion-Channel Function in Real Time through Quantum Decoherence. *Proc. Natl. Acad. Sci. U. S. A.* **2010**, *107*, 18777−18782.
(37) Marseglia, L. In *Photonic Crystals-Innovative Systems, Lasers and Waveguides*; Massaro, A., Ed.; Intech: Rijeka, Croatia, 2012; Chapter 11.
(38) Nebel, C. E.; Yang, N.; Uetsuka, H.; Osawa, E.; Tokuda, N.; Williams, O. Diamond Nano-Wires, A New Approach Towards Next Generation Electrochemical Gene Sensor Platform. *Diamond Relat. Mater.* **2009**, *18*, 910−917.
(39) Cerna, M.; Holubec, L.; Pesta, M.; Kormunda, S.; Topolcan, O.; Cerny, R. Quantitative Estimation of CEA and CK20 Expression in Tumour Tissue of Colorectal Cancer and its Liver Metastases with Reverse Transcription and Real-time PCR. *Anticancer Res.* **2006**, *26*, 803−808.

(40) Deegan, R. D.; Bakajin, O.; Dupont, T. F.; Huber, G.; Nagel, S. R.; Witten, T. A. Capillary Flow as the Cause of the Ring Stains from Dried Liquid Drops. *Nature* **1997**, *389*, 827−829.
(41) Hu, H.; Larson, R. G. Evaporation of a Sessile Droplet on a Substrate. *J. Phys. Chem. B* **2002**, *106*, 1334−1344.
(42) Spano, F.; Massaro, A.; Blasi, L.; Malerba, M.; Cingolani, R.; Athanassioul, A. In Situ Formation and Size Control of Gold Nanoparticles into Chitosan for Nanocomposite Surfaces with Tailored Wettability. *Langmuir* **2012**, *28*, 3911−3917.
(43) Gelderblom, H.; Marín, Á. G.; Nair, H.; van Houselt, A.; Lefferts, L.; Snoeijer, J. H.; Lohse, D. How Water Droplets Evaporate on a Superhydrophobic Substrate. *Phys. Rev. E* **2011**, *83*, 026306-1−026306-6.
(44) Marín, Á. G.; Gelderblom, H.; Lohse, D.; Snoeijer, J. H. Rush-Hour in Evaporating Coffee Drops. *Phys. Fluids* **2011**, *23*, 091111-1.